2D Materials

Spatial variation of geometry, binding, and electronic properties in the moiré superstructure of MoS_2 on Au(111)

To cite this article: Caio C Silva *et al* 2022 *2D Mater.* **9** 025003

IOP Publishing 2D Mater. 9 (2022) 025003 https://doi.org/10.1088/2053-1583/ac4958

2D Materials

RECEIVED
3 November 2021

REVISED
29 December 2021

ACCEPTED FOR PUBLICATION
7 January 2022

PUBLISHED
26 January 2022

PAPER

Spatial variation of geometry, binding, and electronic properties in the moiré superstructure of MoS_2 on Au(111)

Caio C Silva[1,2,7], **Daniela Dombrowski**[1,2,7], **Nicolae Atodiresei**[3], **Wouter Jolie**[2], **Ferdinand Farwick zum Hagen**[2], **Jiaqi Cai**[2], **Paul T P Ryan**[4,5], **Pardeep K Thakur**[5], **Vasile Caciuc**[3], **Stefan Blügel**[3], **David A Duncan**[5], **Thomas Michely**[2], **Tien-Lin Lee**[5] and **Carsten Busse**[1,2,6,*]

[1] Institut für Materialphysik, Westfälische Wilhelms-Universität Münster, Münster, Germany
[2] II. Physikalisches Institut, Universität zu Köln, Köln, Germany
[3] Peter Grünberg Institut and Institute for Advanced Simulation, FZ Jülich and JARA, Jülich, Germany
[4] Department of Materials, Imperial College London, London, United Kingdom
[5] Diamond Light Source Ltd, Didcot, United Kingdom
[6] Department Physik, Universität Siegen, Germany
[7] Contributed equally.
[*] Author to whom any correspondence should be addressed.

E-mail: carsten.busse@uni-siegen.de

Keywords: transition metal dichalcogenides, molybdenum disulfide, MoS_2, 2D materials, x-ray standing waves, scanning tunneling microscopy, moiré

Abstract

The lattice mismatch between a monolayer of MoS_2 and its Au(111) substrate induces a moiré superstructure. The local variation of the registry between sulfur and gold atoms at the interface leads to a periodic pattern of strongly and weakly interacting regions. In consequence, also the electronic bands show a spatial variation. We use scanning tunneling microscopy and spectroscopy (STM/STS), x-ray photoelectron spectroscopy (XPS) and x-ray standing wave (XSW) for a determination of the geometric and electronic structure. The experimental results are corroborated by density functional theory. We obtain the geometric structure of the supercell with high precision, identify the fraction of interfacial atoms that are strongly interacting with the substrate, and analyze the variation of the electronic structure in dependence of the location within the moiré unit cell and the nature of the band.

1. Introduction

Single layers of transition metal dichalcogenides (TMDCs) form a particularly interesting class of two-dimensional materials: as for their bulk parent compounds, there is a large number of possible compositions with different properties [1] which can also contain metal atoms with large atomic number that induce strong spin–orbit coupling [2]. New properties can arise in monolayers due to the absence of inversion symmetry in the frequently found $2H$-structure and due to quantum confinement. For the semiconductor $2H$-MoS_2 this induces a change of the band gap from indirect to direct with corresponding dramatic changes in optical properties [3] and enables exploitation of the valley degree of freedom [4]. In addition, $2H$-MoS_2 can host quasiparticles as excitons, trions [5], and polaronic trions [6].

As for the whole family of 2D materials, epitaxial growth is a versatile preparation method for TMDCs. The commonly found lattice mismatch between overlayer and substrate can lead to a moiré superstructure: within one moiré unit cell the atoms of the 2D material sit in different positions with respect to the underlying substrate. In each of these regions the binding of the 2D layer to the substrate is different, it can even alternate from physisorbed to chemisorbed [7]. The effects of the moiré superstructure are not limited to pure structural aspects, as the different atomic stacking has a strong influence on the electronic properties as well: band gap and work function can follow the moiré modulation [8]. In special cases, such a periodic potential can induce completely new effects as for example superconductivity in twisted graphene bilayers [9].

The growth of MoS_2 by reactive molecular beam epitaxy (MBE) on metal substrates (foremost

Au(111)) has been studied early on [10] and the preparation recipes have been continuously refined to achieve large crystallites [11, 12] and a unique orientation [13]. The band structure determined by angle-resolved photoemission spectroscopy is characteristic for the 2 *H* polymorph of MoS_2 [12–14]. It turned out that in the presence of the chemically active and polarizable metal surface, effects of hybridization [15] and screening [16, 17] have to be taken into account, leading for example to total quenching of the characteristic photoluminescence signal [18].

Especially in MoS_2/Au(111), the system studied here, moiré-induced changes to the geometric and electronic structure have been observed [13, 15, 19]. Separating structural from electronic effects in this and similar systems is a non-trivial task. Scanning probe techniques such as scanning tunneling and atomic force microscopy (STM/AFM) provide 2D images of the sample surface with atomic resolution. However, in STM measurements the tip follows the contour of constant local density of states, thus electronic and structural contributions are convoluted. In AFM structural and mechanical properties are intertwined. The high spatial resolution of STM makes scanning tunneling spectroscopy (STS) the perfect tool to investigate the electronic structure on atomic scale. However, access to the crystal momentum of the states is limited. Photoemission-based techniques give a global view on electronic properties via the valence electrons and on chemical properties via the core electrons, but lack spatial resolution. In conclusion, several techniques have to be combined to gain a full understanding of both geometric and electronic properties.

In this study, we use the x-ray standing wave technique (XSW), STM/STS, and density functional theory (DFT) calculations in order to disentangle the structural and electronic contributions to the moiré modulation of MoS_2 grown on Au(111). STM gives precise data on the lateral structure, leading to the identification of an 11-on-12 structure as the closest commensurate model of the moiré superstructure, that we use in advanced DFT calculations. We find an apparent contradiction between the corrugation determined by STM and DFT, which motivates our XSW study that is able to determine the vertical distances of the atomic layers with high accuracy. We conclude that the structure observed in STM is dominated by electronic rather than geometric effects. Furthermore, XSW allows identification of the strongly bonded moiré regions. Finally, we use STS to follow the local variations in band structure in the unit cell of the superperiodic structure.

2. Results and discussion

2.1. Geometric structure

We grow MoS_2 on Au(111) by reactive MBE see section 4 for details. The preparation parameters of samples for STM/STS and for XPS/XSW are virtually identical, except that a higher coverage ($\lesssim$1 ML) was used for the photoemission experiments.

Figure 1(a) shows an STM image (see section 4) containing two MoS_2 islands on Au(111). A multicolor scale is used, so that the gold surface (exhibiting the characteristic herringbone reconstruction [20]) appears blue and the MoS_2 islands brown with an apparent height of 1.9 Å. On the islands a hexagonal moiré superstructure is visible, resulting from the superposition of the MoS_2 and Au(111) lattice.

Following previous studies, we identify the islands as MoS_2 nanoflakes of one monolayer height [10–15, 18, 19, 21, 22]. The apparent height of the islands is small compared with the thickness of a single MoS_2 layer as defined by the layer spacing in bulk MoS_2 of 6.147 Å [23]. However, the apparent height determined by STM strongly depends on the electronic structure and can be very different from the geometric height, especially for a semiconducting material as MoS_2. This can be illustrated by the strong dependence of the apparent height of MoS_2 on tunneling voltage [18].

The atomically-resolved STM image in figure 1(b), shows the small scale periodicity of the MoS_2 lattice and the superimposed long range periodicity of the moiré pattern where we label the different regions as top, hcp, and fcc, following [19]. The rationale of this nomenclature will be explained below. LEED (figure 1(c)) displays the characteristic moiré pattern consisting of first order spots of Au(111) and MoS_2, surrounded by satellite spots in a hexagonal arrangement.

LEED indicates the precise alignment of the lattice vectors of MoS_2 and Au(111). In consequence, also the lattice vectors of MoS_2 and those of the moiré superstructure are strictly parallel. This is well visible the STM image in figure 1(b) where even a small misalignment would be well visible due to the amplifying effect of the moiré [24]. Our finding of rotationally aligned growth of MoS_2 on Au(111) is in line with a recent study using spot profile analysis (SPA) LEED [13], a globally averaging technique with high resolution (HR) in reciprocal space.

Figure 1(d) shows the apparent height profile taken along the main diagonal of the moiré cell (gray arrow in figure 1(b)). We find a global maximum at the top and a local maximum at the bridge sites in between fcc and hcp. The peak to peak corrugation varies with tunnel conditions and tip, the largest value we found is ≈1 Å. For bias voltages close to zero the difference between the two minima is rather small. For high positive as well as large negative voltages (≈ ±2 V, not shown) one minimum appears significantly higher, which allows us to identify this region as fcc [19].

We use the moiré pattern to determine the lattice parameters with high precision, and without errors caused by piezo creep, drift, STM calibration

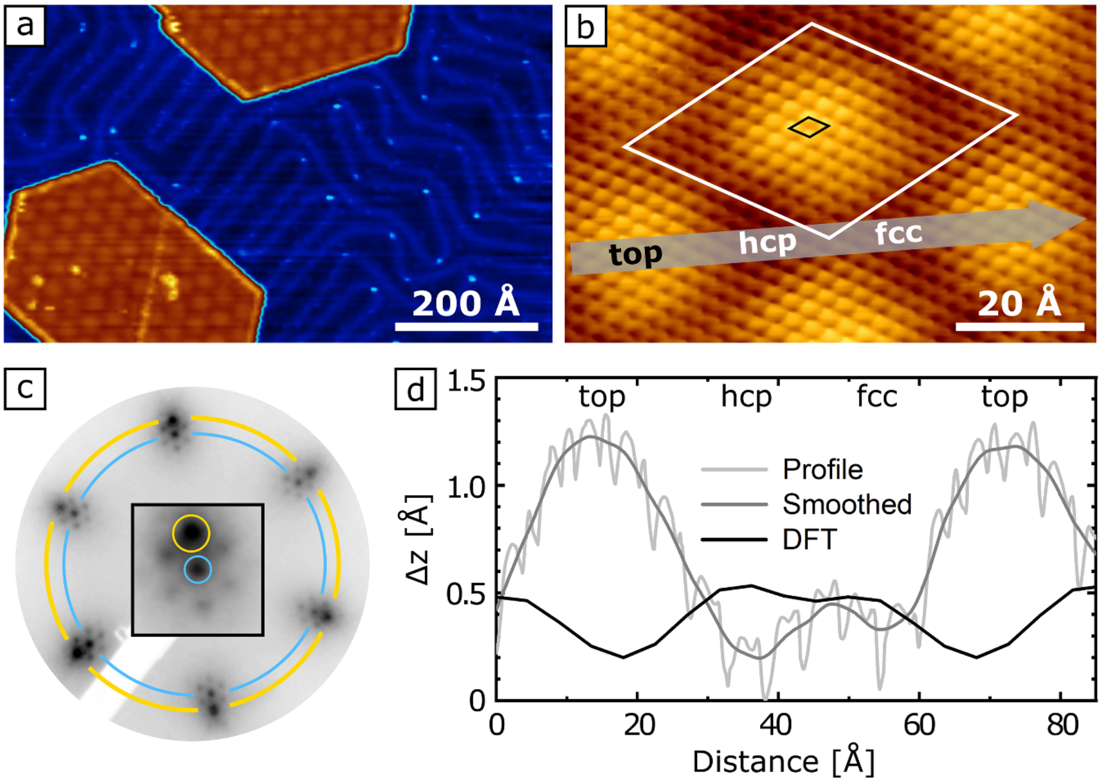

Figure 1. Geometric structure of MoS_2/Au(111). **(a)** STM overview of MoS_2/Au(111) ($I = 440$ pA, $U = -1100$ mV). **(b)** Atomically resolved STM image ($I = 460$ pA, $U = 50$ mV), black diamond: MoS_2 unit cell, white diamond: moiré unit cell. **(c)** LEED pattern (inverted contrast), $E = 150.5$ eV. Blue: MoS_2, yellow: Au(111). **(d)** Profile along gray line in (b) from STM (raw data and smoothed) and DFT, see legend.

or distortion [24]. In the case of precise alignment of both lattices as found here, the moiré unit cell is formed by $(m \times m)$ MoS_2 unit cells on $([m+1] \times [m+1])$ Au(111) unit cells ($a_{\mathrm{Au}} = 2.884$ Å [25]). We find $m = 10.6\ \pm 0.1$ (error is the standard deviation resulting from several measurements at different positions), leading to $a_{\mathrm{MoS_2}} = (3.157\ \ \pm 0.003)$ Å and $a_{\mathrm{moiré}} = (33.3\ \ \pm 0.3)$ Å. The closest commensurate approximation of the moiré cell is $(11\ \ \times 11)$ MoS_2 unit cells on $(12\ \ \times 12)$ Au(111) unit cells, or 11-on-12 for short.

Our lattice constant agrees within error bars with the bulk lattice constant of $a_{\mathrm{MoS_2}} = 3.1602$ Å [23]. The result for the periodicity of the moiré superstructure differs from recent findings. Bana *et al* find a 10-on-11 unit cell by SPA LEED [13]. The discrepancy may be due to difficulties in the calibration of electron diffraction patterns. Tumino *et al* find lattice constants of $a_{\mathrm{MoS_2}} = (3.18\ \ \pm 0.05)$ Å and $a_{\mathrm{moiré}} = (33\ \ \pm 1)$ Å [18] determined via Fourier transformation of a large MoS_2 area, and decided to use a 10-on-11 unit cell in DFT [22]. However, the 11-on-12 supercell is also within their limits of error. Our results have increased accuracy as we take advantage of the magnifying effect of the moiré.

We perform a DFT calculation (see section 4) for one $(11\ \ \times 11)$ MoS_2 layer on top of three $(12\ \ \times 12)$ Au layers. The relaxed structure is shown in figure 2. Three regions of high symmetry (white circles) are evident that we label by the position of S in the lower layer with respect to Au(111), because this determines the local interaction. In the top region S is on top of a gold atom, whereas in the fcc-region (hcp-region) it resides in a threefold-hollow site of fcc (hcp) type. The latter two regions behave very similarly and are often summarized as hollow region. Figure 2(b) shows the side view cut along the main diagonal exposing the $(1\bar{1}0)$ plane. The height of S in the upper layer along this cut is plotted in figure 1(c). It is obvious that the apparent corrugation in STM is inverted and has a larger amplitude. We will show in the following that the apparent height in STM is dominated by electronic effects, meaning that the maxima in the top region are caused by a high local density of states that overcompensates the small distance between MoS_2 and Au(111) in these areas.

The vertical distribution of the atoms is described in table 1. The minimum height of $h_{\mathrm{min}} = 2.50$ Å of the S atoms in the lower layer (S1) is found for the top region. The Mo layer and the upper S layer (S2) follow the lower layer with very similar corrugation. The average thickness of the MoS_2 monolayer (defined as the S-S distance) is 3.11 Å, which is slightly reduced with respect to bulk $2\,H$-MoS_2 (3.19 Å [23]).

The charge density difference in the central $(1\bar{1}0)$ plane is shown in figure 2(c). The regions are

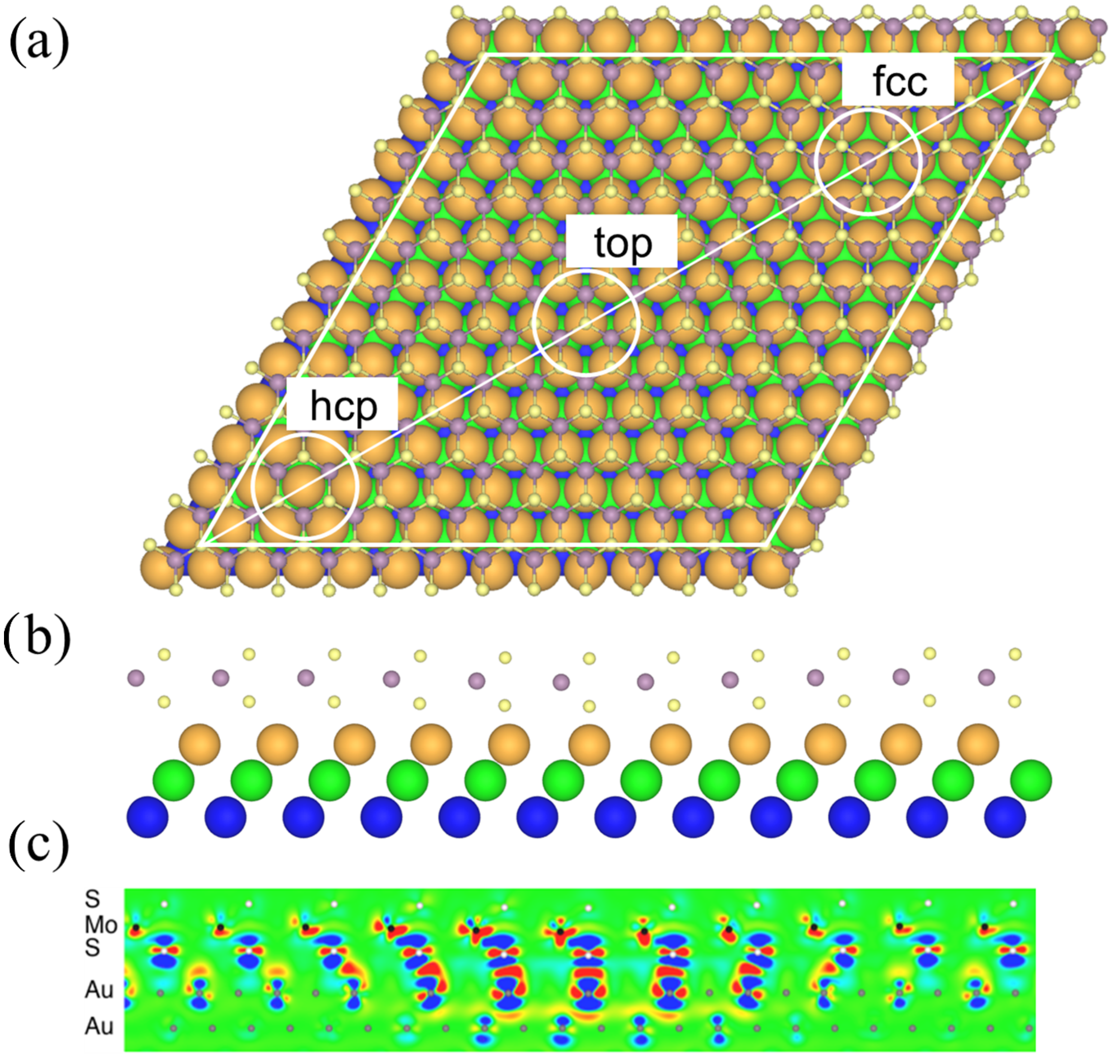

Figure 2. Relaxed structure of 2 H-MoS_2/Au(111) obtained by DFT. (a) Top view. Spheres denote S (yellow), Mo (purple) and Au coded by layer (brown-green-blue). White diamond: $(11\ \times 11)_{MoS_2}/(12\ \times 12)_{Au}$ unit cell, regions of high symmetry are labeled. (b) Side view cut in the $(1\bar{1}0)$ crystallographic plane (main diagonal in (a)). (c) Charge density difference in the same cut as in (b). The isosurface corresponds to 0.008 e^- $Å^{-3}$ with the charge accumulation (depletion) plotted in red (blue). This figure has been generated using VESTA [26].

Table 1. Mean height $\bar{h}$, minimum height h_{min}, maximum height h_{max} and corrugation $\Delta h = h_{\mathrm{max}} - h_{\mathrm{min}}$ of the atoms in the lower (S1) and upper (S2) sulfur layer as well as the Mo layer, referenced to the topmost Au layer. All values in Å.

	S1	Mo	S2
$\bar{h}$	2.72	4.28	5.83
h_{min}	2.50	4.43	5.64
h_{max}	2.87	4.08	5.97
Δh	0.37	0.35	0.33

markedly different: In the top region charge accumulates between S and Au, indicating a chemical bond (chemisorption). The charge stems from the p_z atomic-like orbitals of the S atoms and the d-orbitals of the Au atoms underneath. There is much less charge transfer in the hollow regions. Moreover, the charge accumulation at the hybrid MoS_2-Au(111) interface goes along with a site-dependent charge rearrangement between the interfacial S atoms and the Mo atoms. This rearrangement modulates the strength of S-Mo chemical bond in the MoS_2 layer.

In order to scrutinize the DFT calculation we applied the method of XSW (see section 4 for experimental details). We prepared samples using virtually identical parameters except an increased number of growth cycles leading to a higher coverage (see section 4). The LEED pattern (inset of figure 3(a)) is qualitatively equivalent to the one shown in figure 1(c). The higher coverage of MoS_2 is reflected in the increase of the intensity ratio between MoS_2- and Au-related spots and the increased sharpness of the moiré satellites.

The number of cycles is still low enough to avoid the growth of bilayers [12]. The absence of bilayers is also indicated by the LEED pattern: a significant coverage with bilayers should lead to a decrease of the

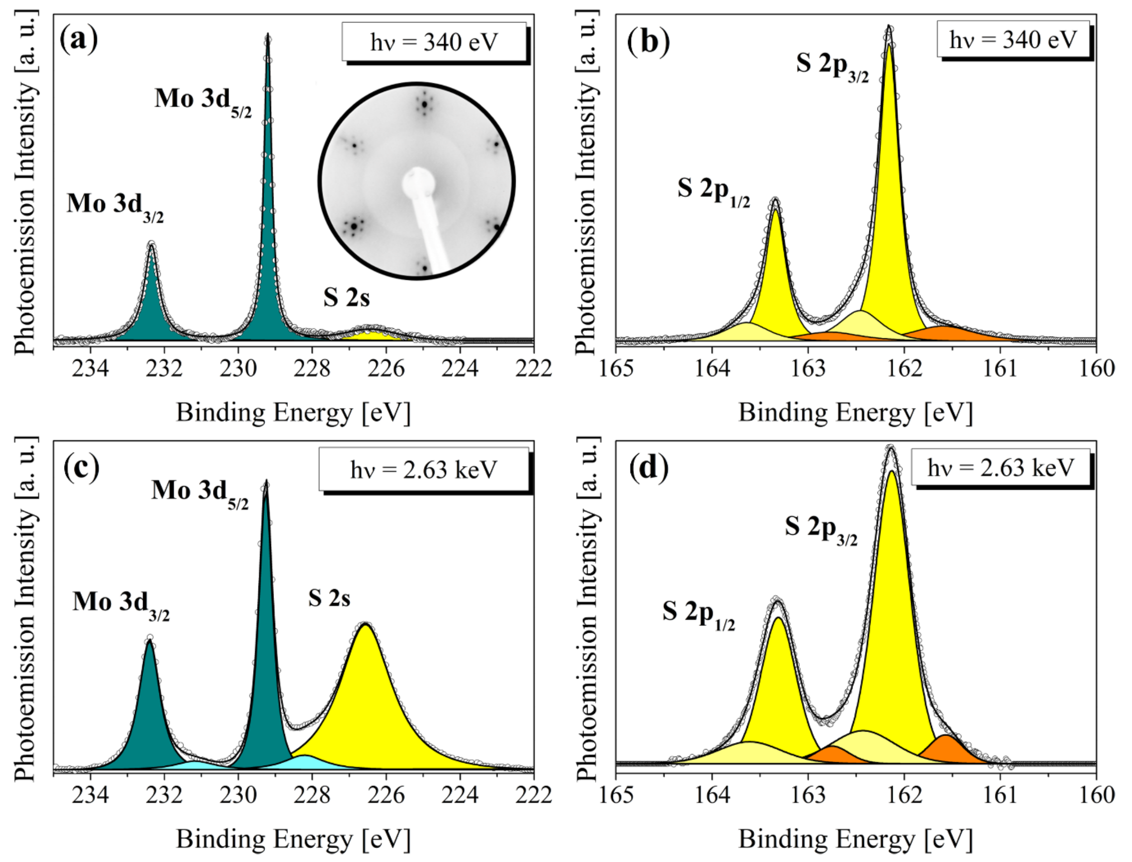

Figure 3. HR-XPS of MoS_2/Au(111). (a) Mo 3d and S 2s (inset: LEED pattern, inverted contrast, $E = 75.5$ eV), (b) S 2p. XPS of (c) Mo 3d and S 2s, (d) S 2p. Circles: data points after background subtraction. Colored areas: fits of the indicated peaks and components (Mo^A 3d: dark cyan, Mo^B 3d: light cyan, S 2s: yellow, S^A 2p: yellow, S^B 2p: light yellow, S^C 2p: orange). Solid black line: sum of fits.

Table 2. Key parameters of the components observed in photoemission (HR-XPS, XPS, and XSW). Binding energy E_B, full width at half maximum Γ, mixing parameter for Voigt-like function β, spin-orbit-splitting Δ_{so}, intensity relative to the most intense component for soft (I_{soft}) and hard (I_{hard}) x-rays. Coherent position P^H ($\Delta P^H = \pm 0.02$) and coherent fraction f^H ($\Delta f^H = \pm 0.04$).

	HR-XPS					XPS	XSW	
Component	E_B (eV)	Γ (eV)	β	Δ_{so} (eV)	I_{soft}	I_{hard}	P^H	f^H
Mo $3d_{5/2}$	229.19	0.26	1.00	3.14	1	1	0.81	0.90
S 2s	226.41	2.00	0.55	—	1	1	0.35	0.39
S^A $2p_{3/2}$	162.16	0.25	0.85	1.18	1	1	0.42	0.50
S^B $2p_{3/2}$	162.46	0.51	0.75	1.18	0.20	0.25	0.07	0.89

moiré satellite spots, as in STM it is found that the moiré superstructure is not present on bilayers [12]. In our experiments, we find the opposite behavior.

Figure 3 shows HR-XPS of the core levels Mo 3d and S 2s (figure 3(a)), as well as S 2p (figure 3(b)). The fitting parameters of the main components are given in table 2. For S 2p we also find a minority component S^C 2 $p_{3/2}$ ($E_B = 161.60$ eV, $\Gamma = 0.75$ eV). As demanded for XSW experiments, a higher incident photon energy of 2.63 keV (off-Bragg condition) has been used for the spectra depicted in figures 3(c) and (d), which changes the photoelectron cross sections and reduces resolution and surface sensitivity (partly compensated by detecting photoelectrons under a more grazing emission angle.) We observe an additional doublet Mo^B 3d at a lower binding energy of 228 eV (light blue in figure 3(c)).

Our highly-resolved spectra are very similar to those presented by Bana *et al* [13], and the fitting parameters are almost identical. This also implies that in both studies the same phase, namely 2 *H*, is present. We observe two additional minor components (Mo^B 3d and S^C 2p) which could be due to differences in the growth procedure. We tentatively attribute S^C 2p to S atoms at the edges of MoS_2 islands with reduced coordination [15]. Mo^B is assigned to metallic Mo on or embedded in Au(111) which was found at the very same binding energy in previous studies [15].

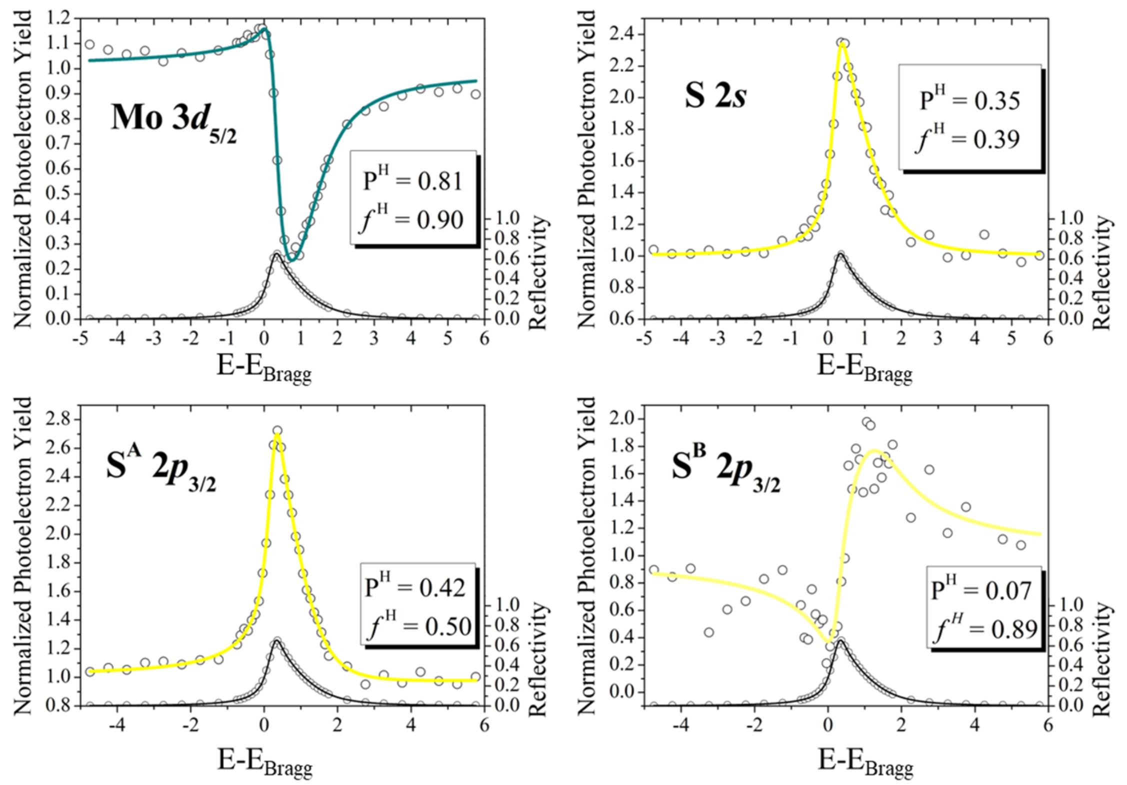

Figure 4. XSW results for MoS$_2$/Au(111). The analysis is presented for each component (Mo^A 3d$_{5/2}$, S 2s , S^A 2p$_{3/2}$ and S^B 2p$_{3/2}$) showing the variation in total photoelectron yield as function of the photon energy scan along the reflectivity curve. The values of coherent position (P^H) and coherent fraction (f^H) are shown to each component analysis.

Table 3. Comparison between the structural parameters determined by XSW for each component and by a model for the assigned species based on DFT. The model is based on an attenuation factor of $\alpha = 0.76$ and a strongly bound fraction of the lower S layer of $f = 0.45$, see text. Experimental values are indicated in bold.

	Component Species	Mo 3d$_{5/2}$ Mo	S 2s S1^h+S1^t+S2	S^A 2p$_{3/2}$ S1^h+S2	S^B 2p$_{3/2}$ S1^t
P^H	**Experiment**	**0.81**	**0.35**	**0.42**	**0.07**
	Model	0.82	0.35	0.41	0.12
f^H	***Experiment***	***0.90***	***0.39***	***0.50***	***0.89***
	Model	*0.97*	*0.53*	*0.66*	*0.98*

We performed an XSW analysis to determine the distribution of Mo and S perpendicular to the surface. In short, such an analysis yields two structural parameters: the coherent position $\left(P^H\right)$ and the coherent fraction $\left(f^H\right)$ [27]. P^H is the average height of all atoms of the analyzed species and f^H indicates the distribution of atoms around this mean height ($f^H = 1$ for a δ-like distribution). The average height of a species is given by $\bar{h} = \left(P^H + n\right) \times d_{\mathrm{Au}(111)}$, where $d_{\mathrm{Au}(111)} = 2.3545$ Å [25] is the Bragg plane spacing of Au(111). The dependence of the photoelectron yield on the x-ray energy for the main Mo 3d$_{5/2}$ peak, the S 2s peak, and the two most intense S 2p$_{3/2}$ peaks is presented in figure 4. The resulting structural parameters coherent position P^H and coherent fraction f^H are given in table 2. However, only for Mo a direct interpretation of these parameters is possible: $P^H = 0.81 \pm 0.02$ yields a mean Mo height of (4.26 ± 0.05) Å above the virtual unrelaxed surface, $f^H = 0.90 \pm 0.04$ indicates a very flat layer. The S components are a convolution of different species, and thus an interpretation is only possible by comparison to the DFT calculation.

Table 3 compares P^H and f^H derived from the DFT-calculated atomic positions (see section 4) with the experiment. For Mo the assignment of the atoms to an atomic species is simple and we obtain a good agreement between theory and experiment, especially for the more robust parameter coherent position: whereas f^H is diminished by thermal disorder as well as by any contamination (adatom, incorporated in bulk, island edges, grain boundaries), such presumably broadly distributed atoms have a negligible effect on P^H.

For sulfur, the comparison is not as simple. First, there are different species of S in MoS$_2$/Au(111), and second, not all photoelectrons from the lower

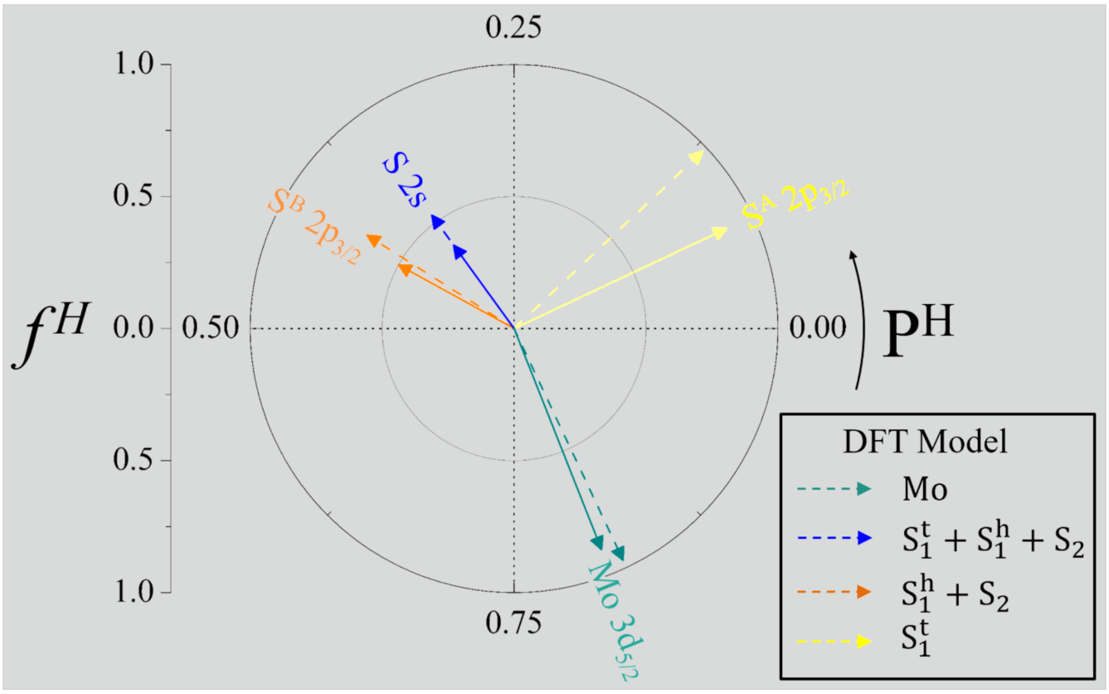

Figure 5. Argand diagram: a vectorial representation combines the coherent positions P^H (polar angle) and coherent fractions f^H (vector length). Solid vectors: XSW results (see labels), dashed vectors: model based on DFT (see legend).

S layer reach the detector due to attenuation by the Mo layer and the upper S layer. We propose a model (guided by DFT) where we distinguish three different species of S: all sulfur atoms in the upper layer belong to one species (S2), but for the lower layer we distinguish two species: a fraction of $(1 - f)$ belongs to $\mathrm{S1^h}$ that are sulfur atoms weakly bound to the gold substrate (S-hollow), and a fraction of f belong to a strongly bound species $\mathrm{S1^t}$ (S-top). We describe the attenuation with a parameter α defined as the fraction of photoelectrons from the lower S layer reaching the detector as compared with the upper one.

We start with the core level S 2s (top-right in figure 4). As the corresponding photoemission peak shows just one component, all sulfur atoms must contribute ($\mathrm{S1^h}$+$\mathrm{S1^t}$+S2). The calculated structural parameters, corresponding to all S atoms present in the DFT model, are $P^H_{\mathrm{S2s}} = 0.32$ and $f^H{}_{\mathrm{S2s}} = 0.51$, clearly deviating from experiment (see table 2). This discrepancy can be solved by taking into account that the weight of the lower S layer is reduced by α due to attenuation. The best description of our experimental data is found using $\alpha = 0.76$.

With $\alpha = 0.76$ it is clear that the XPS component $\mathrm{S^B}$ $2p_{3/2}$ cannot be due to the full lower layer, because in this case its relative intensity should just be $I_{\mathrm{S^B}2p_{3/2}} = \alpha = 0.76$, in clear contrast to the experimental value $I_{\mathrm{S^B}2p_{3/2}} = 0.25$. Under the assumption that only strongly bound atoms of the lower layer ($\mathrm{S1^t}$, fraction f) contribute to the component $\mathrm{S^B}$, while all other S atoms contribute to $\mathrm{S^A}$, we find $I = \frac{\alpha f}{1+\alpha(1-f)}$, yielding $f = 0.45$. In other words, roughly half of the lower S qualify as strongly bond, the other half as weakly bound. Thus one can calculate the structural parameters P^H and f^H corresponding to 45% of S atoms closest to the Au surface as the best model for the component $\mathrm{S^B}$ $2p_{3/2}$, leading to satisfactory agreement (see table 3).

The remaining S atoms contribute to the component $\mathrm{S^A}$ $2p_{3/2}$. Here, both parameters α and f enter in the respective weight of the atoms used to determine P^H and f^H. The good agreement, especially for the coherent position, verifies our approach. Another piece of evidence for our model is the very low coherent fraction of $f^H{}_{\mathrm{S^A}2p_{3/2}} = 0.50$, which cannot be explained in a model that attributes this component to the top layer alone (DFT prediction $f^H{}_{\mathrm{S2}} = 0.97$).

The comparison between the experimental results and the model based on DFT calculations is summarized in an Argand diagram (figure 5). The good agreement validates the DFT calculation and our advanced model. In a complex system as found here, where the same chemical species is present in different layers, an interpretation of the XSW data is only possible by a comparison to a dedicated model as performed here. The failure of a straightforward interpretation of $\mathrm{S^A}$ $2p_{3/2}$ as the upper S1 layer and $\mathrm{S^B}$ $2p_{3/2}$ as the lower S2 layer is directly visible in the Argand diagram: in this case, the symmetry of $\mathrm{MoS_2}$ demands that $\mathrm{Mo^A}$ $3d_{5/2}$ forms the bisector of the two S components, which is clearly not found in experiments.

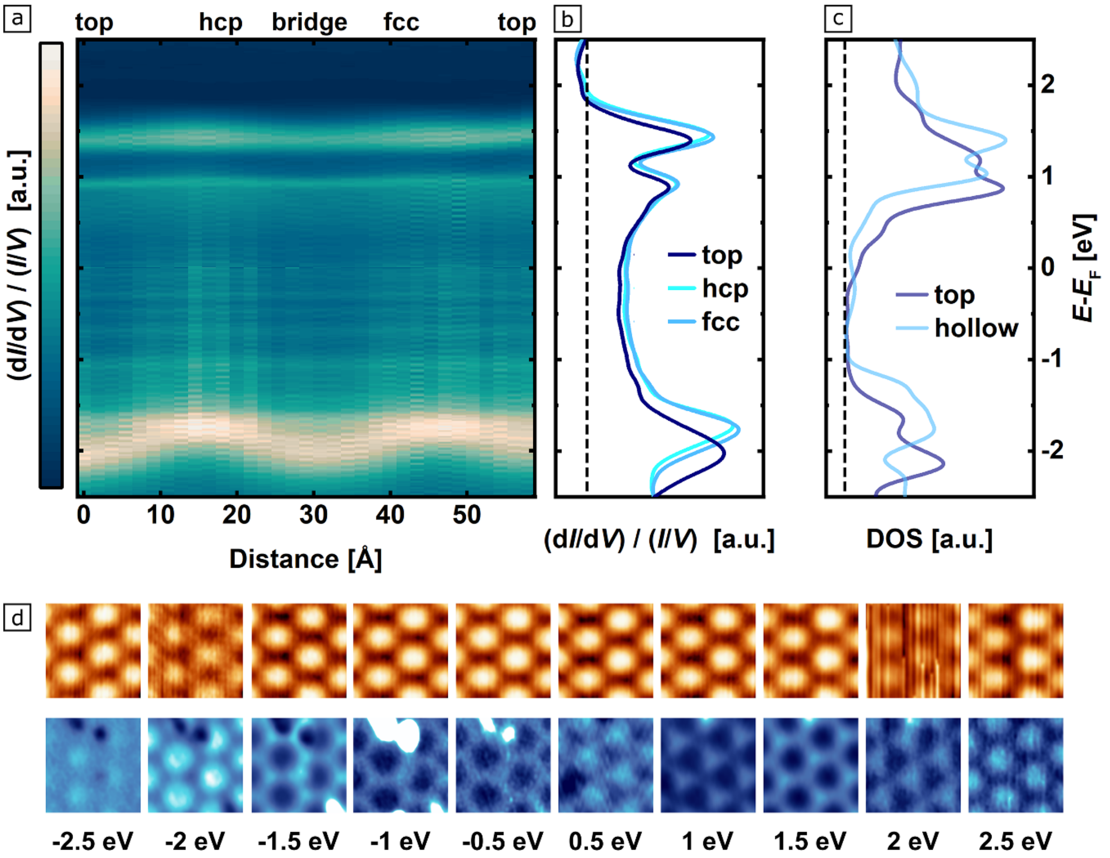

Figure 6. Moiré dependence of the electronic states. (a) Color plot of a line scan over a full moiré unit cell and (b) normalized dI/dV spectra recorded at the high symmetry regions of the moiré pattern. The tip was stabilized at $V = -2.5$ eV and $I = 310$ pA (line scan), $I = 510$ pA (single spectra). (c) Total DOS, summing up the pDOS of s,p,d orbitals. (d) STM and STS maps of MoS_2/Au(111) at different energies. $I = 510$ pA, image size 8 Å × 8 Å.

To reiterate: we observe two main sulfur species in MoS_2 on Au(111). However, the straightforward interpretation that one belongs to the sulfur atoms in close contact with the substrate in the Au-S-Mo-S sequence, and the other one belongs to sulfur atoms at the vacuum side, does not agree with our experimental findings. Instead, we have to distinguish between sulfur atoms in the lower layer that can form a comparatively strong bond to Au atoms due to a favorable on-top-registry (significant chemical shift), and all other sulfur atoms, both in the lower and the upper layer (no chemical shift).

Our assignment of the components forming the S $2p_{3/2}$ peak differs from the one presented in [13]. Whereas in this paper the two peaks are ascribed to the sulfur in the different layers, our data indicates that the distinction is between S strongly bound to Au(111) and nearly undisturbed sulfur atoms from both layers. As the component S^B $2p_{3/2}$ stems exclusively from the lower layer, and the XPS signal from the component S^A $2p_{3/2}$ is dominated by the upper layer, the conclusions drawn from the x-ray photoelectron diffraction (XPD) in [13] may still remain valid.

Comparison of the XP spectra of MoS_2/Au(111) with those of the closely related material TaS_2/Au(111) measures under very similar conditions [28] reveals qualitative differences: in both systems, two main components for the S 2p level are present, but the intensity ratio is much closer to one for TaS_2, where each component could be assigned to a specific S layer. This further supports our model that for MoS_2 the less intense component stems only from a fraction of the S atoms in the lower layer. We speculate that the reason for the different behavior of TaS_2 is its metallic nature that smooths out strong variations in electron density.

In comparison to other epitaxial 2D materials, the MoS_2 layer on Au(111) is rather flat, even though the chemical difference (as evidenced by XPS) between the strongly and weakly bound region is quite pronounced. The strong corrugation observed in STM (up to 1 Å) is completely due to electronic effects, evidencing the difficulty of a precise determination of the vertical structure using scanning probe methods.

2.2. Electronic structure

We use STS to investigate the electronic properties of MoS_2/Au(111) (see section 4). Figure 6(b) shows the spectra in the normalized form $[(dI/dV)/(I/V)]$, where artifacts of voltage and tip-sample separation are reduced [29]. We observe three prominent peaks, one for the occupied states (O1) and two for the

Table 4. Energies of the peaks observed by STS (in eV) for each moiré region. The error, determined by the energy resolution of the STS measurement, is 0.02 eV.

Peak	Top	Fcc	Hcp
O1	−2.02	−1.80	−1.75
E1	0.90	0.92	0.93
E2	1.40	1.44	1.46

empty states (E1, E2). The positions of the peaks depend on the moiré region, see table 4. The peak positions for the fcc and hcp region are very similar, whereas the peaks in the top region are shifted towards lower energies, especially O1.

Our normalized dI/dV spectra are virtually identical to the ones measured in [19], where also O1 (named Q in [19]), E1 (Γ_1), and E2 (Γ_2) are observed. The spectra found in [21] are different. In these studies, the sample was exposed to air between preparation and measurement, which is not the case for our experiments as well as for [19]. By comparing our peak energies with ARPES [14] and the band structure resulting from DFT calculations in a simplified model [21], we assign O1 to the VB minimum at Γ, which ARPES finds at $E = -1.7$ eV. Similarly, we ascribe E2 to the CB minimum at Γ. The assignment for E1 is somewhat more difficult. We find local CB minima at matching energies near M as well as between Γ and Q. Presumably, all these states contribute to E1. However, since the states between Γ and Q have smaller parallel momentum $k_{\|}$, they will dominate the tunneling signal and thus we primarily associate E1 with these states (which are found at significantly higher energy than for freestanding MoS_2).

There is agreement as well as disagreement with the assignment of the peaks by Krane *et al* [19]. The authors based their interpretation on measurements of the decay constant of the tunnel current κ, which contains information on $k_{\|}$ [30]. They find a low value of κ for E2 and higher and mutually similar values for E1 and O1. Consequently, they assign E2 to the minimum of the CB at Γ and O1 to the VB minimum at Q. They do not attribute E1 to a specific state. We follow the assignment for E2, but disagree for O1. The energy of the valence band minimum at Q is determined by ARPES as $E \approx -2.3$ eV [14], which is considerably higher than the energy observed by STS. A much better match is found for the band maximum around Γ at $E = -1.7$ eV, which appears very broad and diffuse in ARPES. DFT calculations show that the maximum of a singular band observed for free-standing MoS_2 is destroyed by hybridization with Au(111). Instead new band extrema in the vicinity of Γ appear (approximately halfway between Γ and Q, see figure 5 of [21]), which can explain the value of κ . Therefore, we assign O1 to these new hybridization states near Γ.

We map the electronic structure across one moiré unit cell by taking dI/dV spectra at several points along the main diagonal of the moiré cell (see gray line in figure 1(b)) and display them as a color plot (figure 6(a)). The positions of the peaks shift within the moiré structure, especially for O1. In agreement with the point spectra, we observe maxima at the fcc and hcp positions and minima at the top position. Furthermore, we find additional minima at the bridge position, which is at a similar energy as for the top position.

Figure 6(c) shows the DOS calculated by DFT for top and fcc/hcp hollow moiré regions. Two prominent peaks for the empty states, which correlate to E1 and E2, are visible. The peak with the highest intensity in the occupied states can be associated with O1. There are additional peaks, particularly for the conduction and valence band onsets at K, that are not or only faintly visible in dI/dV spectra. Furthermore, the DOS of the top area is shifted compared to the DOS of the hollow sites, in the same direction as in experiment.

In agreement with experiment, the shift is largest for O1 and smallest for E1. The shift is significantly larger than the experimentally observed shift, especially for E1 and E2, but not rigid. This discrepancy may be caused by including the vdW interaction in our DFT calculations as a correction term, which improves the structural results, but does not act on the electronic properties.

The energy of O1 is strongly modulated by the moiré structure as already indicated in [19]. We attribute this modulation to the varying degree of hybridization between this state and states of the substrate. The overlap of the corresponding orbitals is not a simple function of the S-Au distance as the energy of O1 at the bridge position is similar to the one at the top position, even though the local MoS_2 height is very different (see figure 1(c)). The interaction is rather determined by the relative position of the lowest S atoms towards the surface Au atoms and the involved orbitals (S p_z and Au d_{z^2}): if the dense packed S atomic rows are in phase with the dense packed rows of the Au surface (top and bridge regions), the interaction is strongest. In the fcc and hcp moiré areas the S p_z-orbitals point into the fcc and hcp gaps of the Au surface. Correspondingly, the impact is strongest for O1, since the VB edge at Γ is foremost of out-of-plane (S p_z, Mo $4d_{z^2}$) orbital character [21, 31]. In contrast, the CB at Γ (E2) mostly originates from in-plane (S p_x, p_y) orbitals, thus interacting less strongly with the substrate (or their interaction depends less strongly on the local registry) and stays at nearly constant energy.

In addition to dI/dV point spectra we map the electronic effects of the moiré potential at different energies (figure 6(d)). While there are certainly subtle changes in the STM images (as discussed in [19]), more significant differences are found in the STS maps. The relative intensity of the top, hcp and fcc regions strongly depends on the bias voltage. Most obvious are four contrast inversions between top and hollow moiré sites: between -2 eV and -1.5 eV the contrast changes from bright top and dark hollow to dark top and bright hollow areas. The next contrast inversion happens between -0.5 eV and 0.5 eV in reversed order. At 1.5 eV the top areas again appear dark surrounded by a network of bright hollow regions. The contrast changes back to bright top and dark hollow regions at 2.5 eV. The contrast inversions are accompanied by slight changes in the intensity distribution of fcc and hcp sites. At 1 and 2 eV all intensity is focused on fcc (downward pointing triangles) and hcp sites (upward pointing triangles), respectively.

The contrast inversion between -2 and -1.5 eV reflects the shift of O1. The nuanced changes at positive bias voltages reveal a more complex influence of the moiré pattern to the conduction band states, in agreement with subtle changes found in constant current $(\partial I/\partial V)_I$ spectra by Krane *et al* [19].

The apparent height profile of the moiré corrugation measured with STM and the height profile calculated with DFT are exactly inverted. Whereas STM finds a strong corrugation with high top and low hollow regions, DFT predict a very low corrugation with low top and high hollow regions, in agreement with XSW results. Spatially depended STS measurements reveal that the moiré corrugation observed in STM is a pure electronic effect and we attribute the moiré modulation to the varying degree of hybridization between states of the bottom S atoms and substrate states.

The spatial variation of O1 also explains the diffuse appearance of the VB maximum at Γ in ARPES [14]. Our $\mathrm{d}I/\mathrm{d}V$ spectra exhibit a well defined peak for O1, showing that locally the state is well-defined. The key effect behind the broadening is the moiré dependent modulation of the substrate interaction. Since the ARPES signal is averaged over several moiré unit cells, these local variation of the VB maximum can not be resolved.

An alternative explanation of the peak shifts could be based on screening of MoS_2 states by the highly polarizable metal substrate [16, 17], which becomes stronger with decreasing height of the MoS_2. Screening is expected to move states towards the Fermi level. However, for O1 we observe the opposite behavior as it moves away from E_F when we go from the weakly to the strongly bonded regions. This implies that screening effects are not significant in our system.

3. Conclusion

In conclusion, our moiré analysis yields highly precise values for the lattice constant of MoS_2/Au(111), indicating that 11-on-12 is the best commensurate approximation. We perform DFT calculations using a realistically large unit cell and including non-local interactions that are substantiated by a good match with XSW measurements. Thereby, we can show that the apparent corrugation observed in STM is inverted with respect to the actual height of the atoms. In addition, the 2D layer is very flat, in contrast to its appearance in STM. DFT calculation reveals that hybridization between S orbitals and states of the substrates is the main contribution to the bonding. As this hybridization shows a spatial variation across the unit cell, specific regions of the MoS_2 (top regions) are strongly bonded, whereas others (hollow regions) interact only weakly. This leads to the occurrence of different components for S atoms in photoelectron spectra that we could unambiguously attribute to specific species of S. Our STS measurement revealed pronounced changes of the electronic structure across the unit cell that are caused by the variation in hybridization rather than by screening. We could assign all observed peaks to specific electronic states of MoS_2.

4. Methods

We used ultra-high vacuum systems located in Köln, Germany (Createc Fischer, base pressure $P = 1 \times 10^{-10}$ mbar) for STM/STS, and at Diamond Light Source, UK (DLS, [32], $P = 2 \times 10^{-10}$ mbar) for XPS/XSW.

Prior to growth, clean Au(111) was prepared by 1.5 keV Ar^+ sputtering and annealing to 973 K (Köln) (873 K (DLS)). Cleanliness was verified by LEED. MoS_2 was prepared *in situ* following the procedure described in [11] and [12]: Mo was evaporated with a rate of ≈ 0.05 Å min^{-1} (calibrated with a quartz crystal microbalance) for 5 min using an e-beam evaporator (SPECS EBE-4 (OAR EGN4)) with the sample at room temperature. In parallel, the sample was exposed to H_2S using a tube of 12 mm diameter ending 20 mm in front of the sample, resulting in a background pressure of 5×10^{-6} mbar. After the evaporation is stopped, the sample is annealed for 30 min at 853 K (843 K) while the exposure to H_2S is continued. The exposure was stopped directly (5 min) after the heating. A full preparation consisted of one (four) of such cycles.

Electron diffraction patterns were obtained by an MCP LEED (K) and a standard LEED optics (DLS). Images recorded with the MCP LEED need to be corrected for distortions caused by the planar arrangement of the microchannel plates. Correction is done with the program MCPdeskew [33], details of the correction procedure and the required geometric parameters are found in [34].

STM and STS measurements are carried out at 5 K in a chamber separated from the growth chamber (sample transfer under UHV) with a background pressure lower than 10^{-11} mbar. The $\mathrm{d}I/\mathrm{d}V$ point spectra and constant energy maps are recorded using the lock-in technique (modulation frequency

777.3 Hz, time constant 30 ms). The modulation amplitude was 10 mV, providing an energy resolution of 20 meV [35]. An etched tungsten tip is used for all measurements, which is prepared *in situ* by dipping the tip into the gold substrate and measuring the Au(111) surface state [36] to ensure the sensitivity to the LDOS. STM images and STS maps are analyzed with the SPIP software [37].

The XPS and XSW experiments were performed in the end-station of the I09 beamline at DLS (sample transfer under UHV). To combine different techniques, the beamline was designed to provide both soft (100–2100 eV) and hard (2.1–20 keV) x-rays, which are directed to the same spot on the sample. The end-station is equipped with a hemispherical electron analyzer (VG Scienta EW400 HAXPES) with a 17 frame/s CCD camera, having an angular acceptance of 56°. The HR-XPS data were acquired at an emission angle $\theta = 30^\circ$ and a photon energy of $h\nu =$ 340 eV. For the fitting of HR-XPS data, a Shirley-type background [38] was subtracted and the core-level peaks were adjusted by a sum of Voigt-like functions characterized by a mixing parameter β ($\beta = 1$ for pure Lorentzian) as described in our previous work [39]. For Mo $3d_{5/2}$ and Mo $3d_{3/2}$ the mixing parameter was 1 indicating a pure Lorentzian function. The values of spin–orbit splitting were initially constrained to 3.15 and 1.20 eV for Mo 3d and S 2p, respectively. The values shown in table 2 are the optimized values after the fitting process. Errors in the binding energy determination were estimated as $\Delta E_\mathrm{b} = \pm 0.02$ eV.

The XSW measurements were performed in backscattering geometry using the (111) Bragg reflection of Au(111). Photoelectrons from core levels Mo 3d, 2s and S 2p were acquired during the scan of the photon energy around the Bragg energy $E_\mathrm{Bragg} =$ 2.635 keV with $\theta \sim 90^\circ$. This configuration allows us to treat the non-dipolar contributions from the photoelectron yield in the same manner as in our prior work [40]. The model applied to the photoemission spectra obtained during the XSW experiment was based on the fitting of HR-XPS data. Thus, the difference in binding energy between the peak components was constrained to the values found in HR-XPS. Furthermore, during the XSW analysis, the width of peak components were constrained in order to avoid changes in the components' intensities other than those caused by the standing wave effect. The analysis of the dependence of the photoelectron yield on incident photon energy, described by the dynamical theory of x-ray diffraction, results in the structural parameters P^H (coherent position) and f^H (coherent position) [27, 41]. P^H is the Fourier-averaged position of all atoms of the analyzed species relative to the lattice planes of the substrate and f^H describes the distribution of atoms around the position given by P^H. The distance between the center of the height distribution for all analyzed atoms and the substrate lattice plane is given by $d_H = d_{\mathrm{Au}(111)} \times (1 + P^H)$, where $d_{\mathrm{Au}(111)} =$ 2.3545 Å [25] is the Au(111) Bragg plane spacing. The errors of XSW measurements are determined following Mercurio *et al* [42].

Our DFT [43, 44] calculations have been carried out using pseudopotentials generated with the projector augmented wave method (PAW) [45] as implemented in the VASP code [46–48]. The moiré structure of MoS_2/Au(111) was modeled by a slab made of three Au atomic layers with an (11×11) MoS_2/(12×12) Au(111) in-plane unit cell amounting to a total of 795 atoms. With the Brillouin zone sampled by the Γ-point and a cutoff energy of 500 eV, the ground-state geometry of this moiré cell was obtained by relaxing the atomic degrees of freedom of the MoS_2 and the first Au surface layer with a threshold value of the calculated forces of 20 meV $Å^{-1}$. Furthermore, the non-local correlations effects responsible for the van der Waals (vdW) interactions acting between MoS_2 and Au(111) were described with the help of the vdW-DF2 functional [49] together with the exchange energy functional proposed by Hamada [50].

The structural parameters P^H and f^H connected to the DFT model were calculated by using the atomic coordinates resulting from the optimized relaxation in the equations (3.6)–(3.13) of [27].

Data availability statement

The data that support the findings of this study are available upon reasonable request from the authors.

Acknowledgments

The authors gratefully acknowledge the Gauss Centre for Supercomputing (GCS) for providing computing time through the John von Neumann Institute for Computing (NIC) on the GCS share of the supercomputer JURECA at Jülich Supercomputing Centre (JSC). V C, S B and N A gratefully acknowledge financial support from the Deutsche Forschungsgemeinschaft (DFG) through the Collaborative Research Center SFB 1238 (Project No. C01). We acknowledge Diamond Light Source for the award of beam times (SI14799-1, SI16710-1, and SI19801-1). P T P R was supported by the Advanced Characterisation of Materials (ACM) CDT. We acknowledge fruitful discussions with M. Rohlfing (Münster).

ORCID iDs

David A Duncan https://orcid.org/0000-0002-0827-2022
Carsten Busse https://orcid.org/0000-0001-5522-0578

References

[1] Chhowalla M, Shin H S, Eda G, Li L J, Loh K P and Zhang H 2013 The chemistry of two-dimensional layered transition metal dichalcogenide nanosheets *Nat. Chem.* **5** 263

[2] Xiao D, Liu G-B, Feng W, Xu X and Yao W 2012 Coupled spin and valley physics in monolayers of MoS_2 and other group-VI dichalcogenides *Phys. Rev. Lett.* **108** 196802

[3] Mak K F, Lee C, Hone J, Shan J and Heinz T F 2010 Atomically thin MoS_2: a new direct-gap semiconductor *Phys. Rev. Lett.* **105** 136805

[4] Mak K F, He K, Shan J and Heinz T F 2012 Control of valley polarization in monolayer MoS_2 by optical helicity *Nat. Nanotechnol.* **7** 494

[5] Mak K F and Shan J 2016 Photonics and optoelectronics of 2D semiconductor transition metal dichalcogenides *Nat. Photon.* **10** 216

[6] Trushin M *et al* 2020 Evidence of rotational Fröhlich coupling in polaronic trions *Phys. Rev. Lett.* **125** 086803

[7] Busse C *et al* 2011 Graphene on Ir(111): physisorption with chemical modulation *Phys. Rev. Lett.* **107** 036101

[8] Zhang Q, Yu J, Ebert P, Zhang C, Pan C-R, Chou M-Y, Shih C-K, Zeng C and Yuan S 2018 Tuning band gap and work funktion modulations in monolayer hBN/Cu(111) heterostructures with moiré patterns *ACS Nano* **12** 9355

[9] Cao Y, Fatemi V, Fang S, Watanabe K, Taniguchi T, Kaxiras E and Jarillo-Herrero P 2018 Unconventional superconductivity in magic-angle graphene superlattices *Nature* **556** 43

[10] Helveg S, Lauritsen J V, Laegsgaard E, Stensgaard I, Norskov J K, Clausen B S, Topsoe H and Besenbacher F 2000 Atomic-scale structure of single-layer MoS_2 nanoclusters *Phys. Rev. Lett.* **84** 951

[11] Sorensen S G, Füchtbauer H G, Tuxen A K, Walton A S and Lauritsen J V 2014 Structure and electronic properties of in situ synthesized single-layer MoS_2 on a gold surface *ACS Nano* **8** 6788

[12] Grønborg S S, Ulstrup S, Bianchi M, Dendzik M, Sanders C E, Lauritsen J V, Hofmann P and Miwa J A 2015 Synthesis of epitaxial single-layer MoS_2 on Au(111) *Langmuir* **31** 9700

[13] Bana H *et al* 2018 Epitaxial growth of single-orientation high-quality MoS_2 monolayers *2D Mater.* **5** 035012

[14] Miwa J A, Ulstrup S, Sorensen S G, Dendzik M, GrubišićČabo A, Bianchi M, Lauritsen J V and Hofmann P 2015 Electronic structure of epitaxial single-layer MoS_2 *Phys. Rev. Lett.* **114** 046802

[15] Bruix A, Füchtbauer H G, Tuxen A K, Walton A S, Andersen M, Porsgaard S, Besenbacher F, Hammer B and Lauritsen J V 2015 In situ detection of active edge sites in single-layer MoS_2 catalysts *ACS Nano* **9** 9322

[16] Rösner M, Steinke C, Lorke M, Gies C, Jahnke F and Wehling T O 2016 Two-dimensional heterojunctions from nonlocal manipulations of the interactions *Nano Lett.* **16** 2322

[17] Drüppel M, Deilmann T, Krüger P and Rohlfing M 2017 Diversity of trion states and substrate effects in the optical properties of an MoS_2 monolayer *Nat. Commun.* **8** 2117

[18] Tumino F, Casari C S, Bassi A L, Passoni M and Russo V 2019 Pulsed laser deposition of single-layer MoS_2 on Au(111): from nanosized crystals to large-area films *Nanoscale Adv.* **1** 643

[19] Krane N, Lotze C and Franke K J 2018 Moiré structure of MoS_2 on Au(111): local structural and electronic properties *Surf. Sci.* **678** 136

[20] Barth J V, Brune H and Ertl G 1990 Scanning tunneling microscopy observations on the reconstructed Au(111) surface: atomic structure, long-range superstructure, rotational domains and surface defects *Phys. Rev.* B **42** 9307

[21] Bruix A *et al* 2016 Single-layer MoS_2 on Au(111): band gap renormalization and substrate interaction *Phys. Rev.* B **93** 165422

[22] Tumino F, Casari C S, Bassi A L and Tosoni S 2020 Nature of point defects in single-layer MoS_2 supported on Au(111) *J. Phys. Chem.* C **124** 12414

[23] Wilson J A and Yoffe A D 1969 The transition metal dichalocogenides discussion and interpretation of the observed optical, electrical and structural properties *Adv. Phys.* **18** 193

[24] N'Diaye A T, Coraux J, Plasa T N, Busse C and Michely T 2008 Structure of epitaxial graphene on Ir(111) *New J. Phys.* **10** 043033

[25] Maeland A and Flanagan T B 1964 Lattice spacings of gold–palladium alloys *Can. J. Phys.* **42** 2364

[26] Momma K and Izumi F 2011 VESTA 3 for three-dimensional visualization of crystal, volumetric and morphology data *J. Appl. Cryst.* **44** 1272

[27] Zegenhagen J 1993 Surface structure determination with x-ray standing waves *Surf. Sci. Rep.* **18** 202

[28] Silva C C *et al* 2021 Structure of monolayer 2H-Tas_2 on Au(111) *Phys. Rev.* B **104** 205414

[29] Feenstra R M, Stroscio J A and Fein A P 1987 Tunneling spectroscopy of the Si(111)2x1 surface *Surf. Sci.* **181** 295

[30] Zhang C, Chen Y, Johnson A, Li M-Y, Li L-J, Mende P C, Feenstra R M and Shih C-K 2015 Probing critical point energies of transition metal dichalcogenides: surprising indirect gap of single layer WSe_2 *Nano Lett.* **15** 6494

[31] Cappelluti E, Roladán R, Silva-Guillén J A, Ordejón F and Guinea P 2013 Tight-binding model and direct-gap/indirect-gap transition in single-layer and multilayer MoS_2 *Phys. Rev.* B **88** 075409

[32] Lee T-L and Duncan D A 2018 A two-color beamline for electron spectroscopies at diamond light source *Synchrotron Radiat. News* **31** 16

[33] Ikonomov J 2011 private communication

[34] Runte S. 2013 Atomic and electronic structure of graphene and graphene intercalation compounds *PhD Thesis* Universität zu Köln

[35] Morgenstern M 2003 Probing the local density of states of dilute electron systems in different dimensions *Surf. Rev. Lett.* **10** 933

[36] Chen W, Madhavan V, Jamneala T and Crommie M F 1998 Scanning tunneling microscopy observation of an electronic superlattice at the surface of clean gold *Phys. Rev. Lett.* **80** 1469

[37] Image Metrology 2013 SPIP

[38] Shirley D A 1972 High-resolution x-ray photoemission spectrum of the valence bands of gold *Phys. Rev.* B **5** 4709

[39] Farwick zum Hagen F H *et al* 2016 Structure and growth of hexagonal boron nitride on Ir(111) *ACS Nano* **10** 11012

[40] Silva C C *et al* 2018 Valleys and Hills of Graphene on Ru (0001) *J. Phys. Chem.* C **122** 18554

[41] Woodruff D P 2005 Surface structure determination using x-ray standing waves *Rep. Prog. Phys.* **68** 743

[42] Mercurio G *et al* 2013 Adsorption height determination of nonequivalent C and O species of PTCDA on Ag(110) using x-ray standing waves *Phys. Rev.* B **87** 045421

[43] Hohenberg P and Kohn W 1964 Inhomogeneous electron gas *Phys. Rev.* **136** B864

[44] Kohn W and Sham L J 1965 Self-consistent equations including exchange and correlation effects *Phys. Rev.* **140** A1133

[45] Blöchl P E 1994 Projector augmented-wave method *Phys. Rev.* B **50** 17953

[46] Kresse G and Hafner J 1993 Ab initio molecular dynamics for liquid metals *Phys. Rev.* B **47** 558

[47] Kresse G and Furthmüller J 1996 Efficient iterative schemes for *ab initio* total-energy calculations using a plane-wave basis set *Phys. Rev.* B **54** 11169

[48] Kresse G and Joubert D 1999 From ultrasoft pseudopotentials to the projector augmented-wave method *Phys. Rev.* B **59** 1758

[49] Lee K, Murray E D, Kong L, Lundqvist B I and Langreth D C 2010 Higher-accuracy van der Waals density functional *Phys. Rev.* B **82** 081101(R)

[50] Hamada I 2014 Van der Waals density functional made accurate *Phys. Rev.* B **89** 121103(R)